

A diamond voltage imaging microscope

Daniel McCloskey (✉ dan.mccloskey@unimelb.edu.au)

The University of Melbourne <https://orcid.org/0000-0002-4435-4543>

Nikolai Dontschuk

University of Melbourne <https://orcid.org/0000-0001-6061-7537>

Alastair Stacey

RMIT

Charlie Pattinson

The University of Melbourne

Athavan Nadarajah

The University of Melbourne

Liam Hall

The University of Melbourne

Lloyd Hollenberg

The University of Melbourne

Steven Praver

The University of Melbourne

David Simpson

University of Melbourne <https://orcid.org/0000-0001-9056-2469>

Article

Keywords:

Posted Date: May 11th, 2022

DOI: <https://doi.org/10.21203/rs.3.rs-1102242/v1>

License:  This work is licensed under a Creative Commons Attribution 4.0 International License.

[Read Full License](#)

Version of Record: A version of this preprint was published at Nature Photonics on September 8th, 2022.

See the published version at <https://doi.org/10.1038/s41566-022-01064-1>.

A diamond voltage imaging microscope

D. J. McCloskey^{1*†}, N. Dontschuk^{1†}, A. Stacey^{1,2}, C. Pattinson¹, A. Nadarajah¹, L. T. Hall¹, L. C. L. Hollenberg^{1,3}, S. Praver¹, D. A. Simpson^{1*}.

¹School of Physics, University of Melbourne; Parkville, VIC 3010, Australia.

²School of Science, RMIT University; Melbourne, VIC 3001, Australia.

³Centre for Quantum Computation and Communication Technology, School of Physics, University of Melbourne, Parkville, VIC 3010, Australia

*Corresponding author. Email: dan.mccloskey@unimelb.edu.au, simd@unimelb.edu.au

† These authors contributed equally to this work.

Technologies that capture the complex electrical dynamics occurring in biological systems, across fluid membranes and at solid-liquid interfaces drive fundamental understanding and innovation in diverse fields from neuroscience to energy storage. However, the capabilities of existing voltage imaging techniques utilizing micro-electrode arrays, scanning probes, or optical fluorescence methods are respectively limited by resolution, scan speed, and photostability. Here we develop an optoelectronic voltage imaging system which overcomes these limitations by using charge-sensitive fluorescent reporters embedded within a transparent semiconducting diamond device. Electrochemical tuning of the diamond surface termination enables photostable optical voltage imaging with a quantitative linear response at biologically relevant voltages and timescales. This technology represents a major step toward label-free, large-scale, and long-term voltage recording of physical and biological systems with sub-micron resolution.

The development of fluorescent molecular sensors for imaging voltage changes in biological systems has revolutionized neuroscience, providing a tool to capture neuronal activity over large areas with sub-neuron resolution both *in vitro* and *in vivo*¹⁻³. However, the poor photostability of

molecular voltage sensors limits recording times to a few minutes¹⁻⁴, posing problems for longitudinal studies of network evolution and disease processes. These limitations mean that lower-resolution techniques such as multi-electrode arrays (MEAs) remain predominant tools in neuroscientific research^{5,6}, disease modeling, drug discovery and safety pharmacology. By embedding fluorescent, charge-sensitive defects within a transparent semiconducting substrate, solution voltage imaging can in principle be realized by optical detection of local changes in the near-surface semiconductor space-charge layer. Changes to this space-charge layer are known to modulate the fluorescence of the defects by altering the number of electrons bound to each, otherwise known as the charge state of the defect⁷⁻⁹. Such a hybrid optoelectronic approach has been proposed¹⁰ and would occupy a hitherto unexplored voltage imaging regime, combining the spatial resolution of optical techniques with the long-term stability and minimal invasiveness of MEAs. The nitrogen-vacancy (NV) defect in diamond, an atom-scale point defect illustrated in Fig. 1a, is bright¹¹, photostable¹², and possesses three optically distinguishable charge states known to be responsive to voltage changes in solution^{10,13,14}, making it an ideal candidate system for developing this approach. As a substrate, diamond is biocompatible^{15,16} and has well-developed nano-fabrication pathways¹⁷⁻¹⁹, meaning the proposed technique could potentially be applied to both intracellular^{20,21} and extracellular^{16,22} recording. In addition, the chemical inertness of diamond²³ suggests that this approach to voltage imaging could enable time-resolved electrochemical microscopy, complementing the scanning probe techniques currently employed in the characterization of energy storage materials in a wide range of liquid electrolytes^{24,25}.

In this work, we realize optoelectronic voltage imaging with ensembles of NV centers by engineering the near-surface electrostatic environment of diamond for responsiveness to external potentials. We first establish precise electrochemical control of the diamond surface termination,

which we use to tune the ensemble charge state population to an optimal composition for voltage sensing consisting exclusively of the fluorescent neutral (NV^0) and non-fluorescent positive (NV^+) states. This approach minimizes background fluorescence, avoids the spectral overlap between NV^0 and the negative (NV^-) state which would otherwise act to impede sensitivity^{13,26}, and eliminates any requirement for DC biasing¹⁰. We then demonstrate the capabilities of our diamond voltage imaging microscope (DVIM) by performing real-time imaging of capacitive charge injection by a microelectrode in solution. Finally, we show that this sensing mechanism can be replicated and enhanced in an array of diamond nanopillar optrodes, each possessing sub-millisecond fluorescence response times and two orders of magnitude greater voltage sensitivity than previously demonstrated using NV centers^{10,13,14}.

Results

Fabrication and operating principles

Our devices consist of high-density (of order $10^{17}/\text{cm}^3$) ultra-shallow ($\approx 7\text{ nm}$) NV ensembles formed by ion implantation into ultra-pure single-crystal diamond wafers (Methods). The diamonds are hydrogen-terminated by indirect exposure to hydrogen plasma (Supplementary Fig. 1), which prevents hydrogen passivation of shallow NV centers^{27,28} whilst rendering the diamond surface electrically conductive in atmosphere via the formation of a two-dimensional hole gas^{29,30}. The devices are mounted within the custom-built fluid wells illustrated in Fig. 1a, which feature a planar platinum electrode used to apply solution potentials for characterization while fluorescence excitation and collection are simultaneously performed from below. As shown in grey in Fig. 1b, hydrogenation of the diamond surface results in the loss of virtually all detectable fluorescence, indicating full conversion of the NV ensemble to the dark NV^+ state. The charge-state of an NV

center is determined by the position of the Fermi level, E_F , relative to the adiabatic charge-state transition energies illustrated in Fig. 1c. The layer of negatively charged adsorbates which forms on the hydrogenated surface creates a strong electrostatic field that shifts these transition energies upward relative to E_F ³¹, a phenomenon known as near-surface band-bending (NSBB)³⁰. The combination of an ultra-shallow NV ensemble and the low bulk defect concentration of the diamond material used enables surface transfer doping to cause appreciable changes in E_F , forcing it below the $NV^{0/+}$ transition as illustrated in Fig. 1d. Even slightly deeper NV ensembles with the same areal density show some population of NV^0 following hydrogenation (Supplementary Fig. 1), which explains why dense ensembles of NV^+ were previously thought to be intractable¹³.

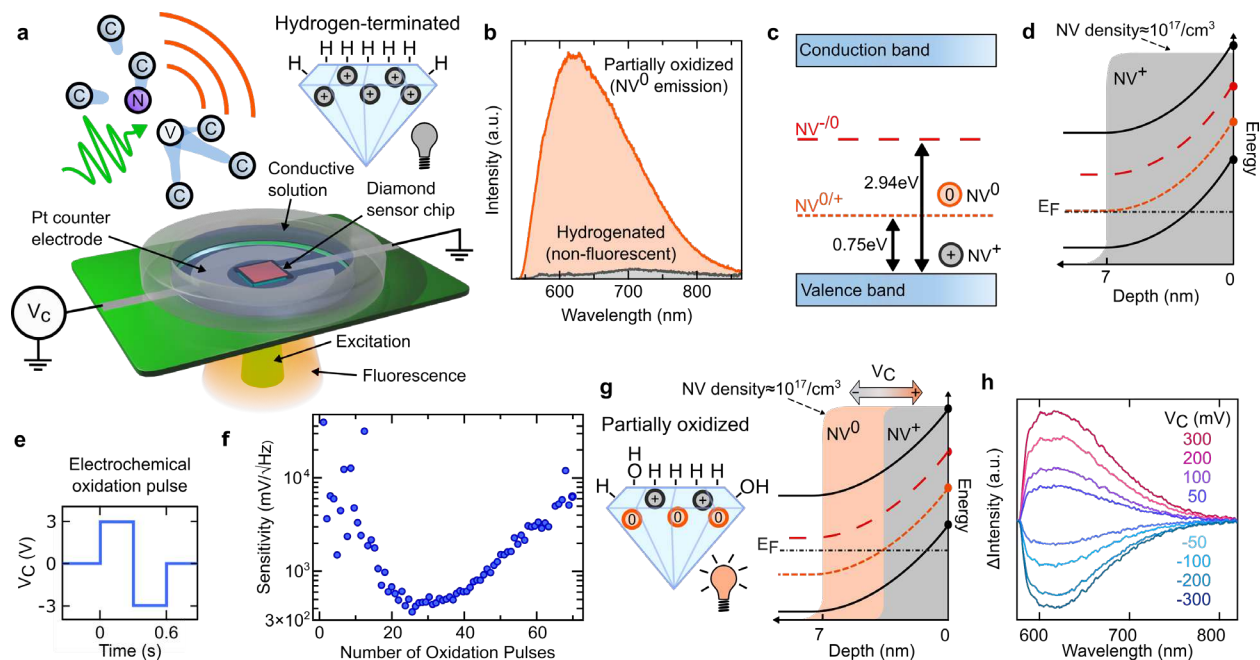


Fig. 1. Principles of diamond voltage imaging microscopy. (a) Illustration of key components used in the sensor design: nitrogen-vacancy (NV) defects, hydrogen termination and transparent fluid well with inert counter electrode for solution gating. (b) Extracted NV fluorescence spectra from a hydrogenated (grey) and partially-oxidized (orange) sample (raw spectra shown in Supplementary Fig. 1) showing the near-complete loss of NV emission following hydrogenation and conversion of the ensemble to the dark NV^+ state, and (c) the relevant NV charge state transition energies relative to the diamond valence band. (d) Schematic of near-surface band-bending and NV charge state

85

population density (solid fill) for hydrogen-terminated diamond. (e) Electrochemical oxidation pulse used to strip a
 90 controlled amount of the hydrogen termination. (f) Voltage sensitivity evolution of a sacrificial diamond sample with
 electrochemical oxidation of the hydrogenated surface. (g) Electronic configuration, and (h) solution gate voltage
 dependence of fluorescence emission of a sensor near optimum sensitivity.

Optimizing the performance of the voltage sensor requires a population of fluorescent NV centers
 whose change in fluorescence in response to an external solution voltage is maximally visible
 95 against their own shot noise. We realize precise control over the NV^0 population by pulsed
 electrochemical oxidation of the diamond surface in phosphate buffered saline (PBS) interleaved
 with *in situ* measurements of voltage sensitivity. Each oxidative voltage pulse, shown in Fig. 1e,
 strips a small fraction of hydrogen atoms from the diamond surface, likely replacing them with
 hydroxyl groups³². This reduces the equilibrium density of negative surface adsorbates and
 100 therefore the NSBB. As the band-bending is incrementally reduced, the population of the bright
 NV^0 state increases (Supplementary Fig. 1) as its adiabatic charge-state transition energy passes
 through the Fermi level at shallower depths³³, which alters the fluorescence response of the device
 to an applied voltage while concurrently increasing the emitted photon shot noise. After each
 oxidative pulse, the voltage sensitivity η is measured and quantified according to (Supplementary
 105 Note 1):

$$\eta = \frac{1}{\beta\sqrt{I_0}} \quad (1)$$

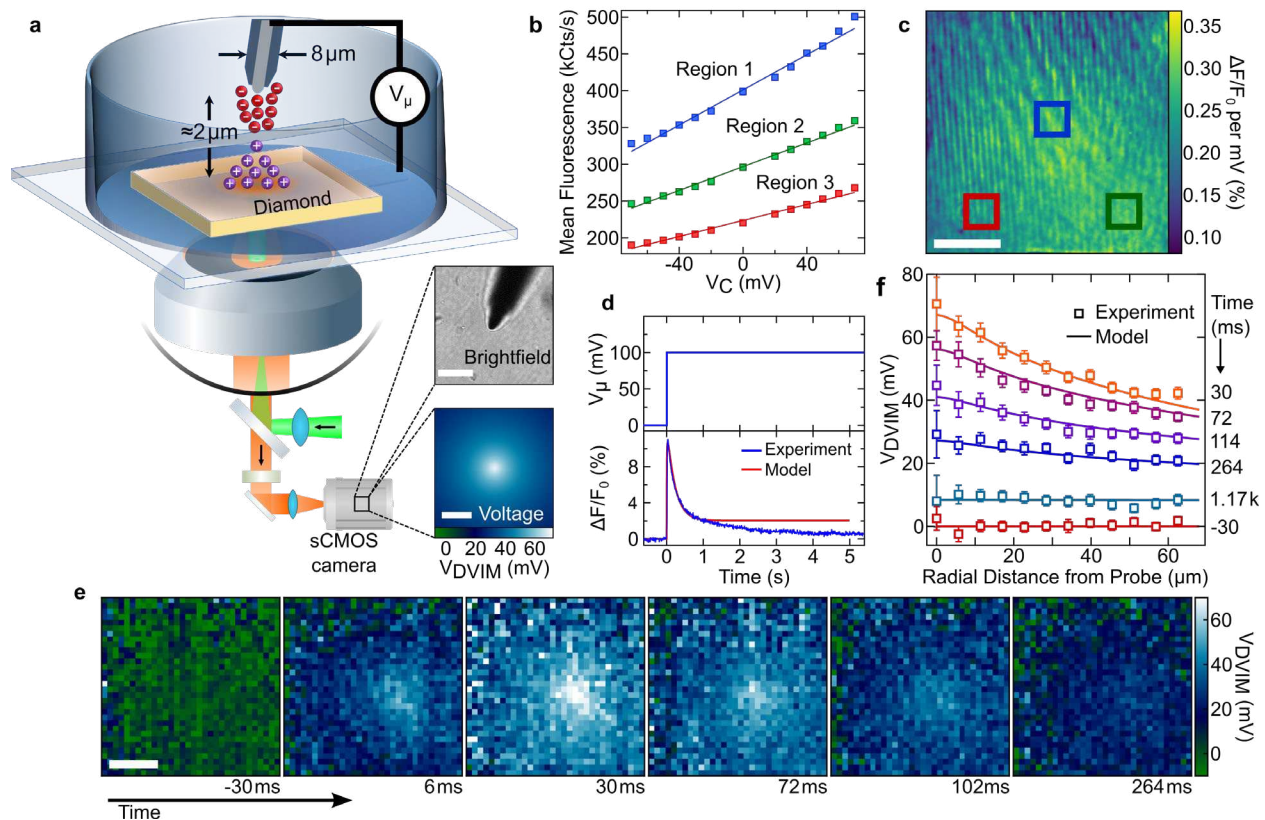
where the fluorescence contrast is estimated with the relation $\Delta I/I_0 = \beta\Delta V$, ΔI is the measured
 change in fluorescence count rate, I_0 is the fluorescence at 0V, and ΔV is the change in solution
 110 potential.

As shown in Fig. 1f, the initial surface oxidation pulses increase the fluorescence contrast and NV^0 population concurrently until the voltage response plateaus in an optimal sensitivity region. At this point the surface is partially oxidized (Fig. 1g, left) with E_F intersecting the $NV^{0/+}$ transition within the shallow implanted region (Fig. 1g, right). The partially oxidized diamond surface retains sufficient conductivity to allow for solvated charges to build up within an electrolytic double-layer (EDL)³⁴ upon application of a solution voltage. As shown experimentally in Fig. 1h, positive solution voltages reduce the upward band-bending, increasing the NV^0 population and fluorescence intensity, while negative solution voltages have the opposite effect. Integrating the raw spectra reveals a fluorescence response which is well approximated by a linear function across a range of gate voltages of around ± 50 mV (Supplementary Fig. 1). For samples oxidized well beyond their maximal sensitivity, we begin to observe $NV^{-/0}$ interconversion (Supplementary Fig. 1). However, the sensitivity of such a configuration is limited by low contrast resulting from spectral overlap between NV^- and NV^0 emissions.

Imaging microelectrode charge injection in solution

To verify the localized solution voltage imaging capabilities of the DVIM, we used it to image the spatiotemporal voltage transient resulting from the application of a voltage step to a proximal microelectrode³⁵. Fig. 2a illustrates the experimental setup: An insulated Pt/Ir microelectrode with an exposed tip diameter of $\approx 8 \mu\text{m}$ (Supplementary Fig. 2) was positioned as close to the diamond surface as possible without contact in a dilute buffered saline solution (Methods). Prior to the measurement of microelectrode signals, the voltage response of the imaged chip area was calibrated using DC voltages applied via the large platinum ring electrode (Methods). Fig. 2b demonstrates the DVIM response within a dynamic range of ± 70 mV, from which linear fits of the responses at each pixel can be used to construct a calibration map as shown in Fig. 2c. A signal

generator was used to apply 100mV between the microelectrode and diamond surface while NV
 135 fluorescence was recorded using an inverted widefield fluorescence microscope and an sCMOS
 camera. This voltage is low enough to ensure the two surfaces behave as ideally polarizable
 electrodes (negligible Faradaic current flows between the two)³². The applied voltage signal and
 corresponding full-frame fluorescence are shown in Fig. 2d.



140 **Fig. 2. Imaging microelectrode charge injection dynamics.** (a) Schematic of the microelectrode and diamond sensor
 arrangement. (b) Relative change in fluorescence vs. solution gate voltage amplitude applied using a large Pt counter
 electrode for three locations on the DVIM surface. (c) A calibration map of the studied region created using the slope
 of the response curve at each pixel. Highlighted squares indicate the regions analyzed in panel (a). (d) Top: The voltage
 step applied to the microelectrode. Bottom: the full-frame measured (blue) and calculated (red) change in fluorescence
 145 following the application of the voltage step. (e) Real-time video recording of changes in local voltage at the diamond
 surface resulting from a 100mV step in the microelectrode potential V_μ . Full video available as Supplementary
 Information. (f) Average voltage measured by the DVIM versus radial distance from the electrode tip for selected

frames. Error bars are 95% confidence intervals of the measured values. Solid lines show a theoretical model of the experiment (Supplementary Methods 1). All scale bars are $50\mu\text{m}$. The camera exposure time was 6ms. These measurements were performed in a dilute saline solution with resistivity $> 20\text{k}\Omega\text{cm}$ (Methods).

At time $t > 0$, positive charge begins to accumulate on the diamond surface directly underneath the microelectrode tip, resulting in increased fluorescence. The maximum at $t = 30\text{ms}$ occurs when the rate at which charge accumulates at the diamond surface is balanced by the rate at which it is laterally transported out of the field-of-view (FOV) by diffusive processes. For $t > 30\text{ms}$, ions continue spreading radially outward until they are evenly distributed across the diamond surface. Select frames showing the localized buildup and subsequent spreading of charge from under the electrode tip are shown in Fig. 2e. These images were captured at 167 frames/sec with an effective pixel mapping of approximately $5.5\mu\text{m}$ and were converted from raw fluorescence images to voltage images using the calibration map in Fig. 2c. Fig. 2f shows radial averages (centered on the microelectrode tip location) of the voltage measured by the DVIM for a selection of times following the voltage step as well as the baseline measurement (red squares, bottom) preceding the step. We found that an equivalent RC circuit model yields very good agreement with our measurements, providing verification that the DVIM accurately reports the underlying solution charge dynamics. Our model (Supplementary Methods 1) contains three parameters: the bulk solution resistivity κ_S , the diamond surface capacitance C_D , and a specific surface resistance accounting for the tangential flow of charge along the diamond surface κ_D . These parameters were varied to fit the simulated time dynamics, shown in Figs. 2d (red line) and 2f (solid lines), to the experimental results. Values of $C_D = 2.3\mu\text{F}/\text{cm}^2$, $\kappa_D = 21\text{M}\Omega$ and $\kappa_S = 42\text{k}\Omega\cdot\text{cm}$ resulted in the best fit to the data. These values are consistent with the previously published estimate for the interfacial capacitance of hydrogenated single-crystal diamond in aqueous electrolyte solution³⁶ of

$2\mu\text{F}/\text{cm}^2$ and the bulk resistivities of $25 - 200\text{k}\Omega\cdot\text{cm}$ which we measured from similar solution preparations to that employed here.

Characterization of a DVIM enhanced by photonic surface structuring

Using equation (1), we determine a median per-area sensitivity for the diamond surface of $482\mu\text{V}\cdot\mu\text{m}/\sqrt{\text{Hz}}$. To enhance the voltage sensitivity, we implement a straightforward approach for increasing light collection by patterning the DVIM surfaces with arrays of nanopillars to act as fluorescence waveguides¹⁹. Fig. 3a shows a scanning-electron micrograph of a diamond sensor surface with an array of 700nm diameter pillars produced by reactive-ion etching (Methods). As evidenced by Fig. 3b, these diamond ‘optrodes’ provide a 10-fold increase in photon collection efficiency from our shallow NV^0 ensembles. Variations in fluorescence intensity from the optrodes shown in the image result from variations in widefield laser excitation, as confirmed by the uniform brightness of the optrodes when observed with scanning confocal microscopy (Supplementary Fig. 3). Fig. 3c demonstrates the photostability of the optrodes, with no degradation of the fluorescence signal amplitude detected over 40 seconds of continuous recording while a 20mV square wave was applied to the sample in PBS using the platinum ring electrode. We also note that no degradation of sensing performance was observed over the period during which the measurements of this device were performed (> 4 months, Supplementary Fig. 4). We confirmed that linearity of the sensor response was preserved following nanofabrication both at the single optrode level and over the aggregate field of view (Supplementary Fig. 3). We observed an increase in the overall fluorescence contrast of the optrodes, shown in Fig. 3d, when compared to the flat surface. This effect was confirmed by measuring the voltage responses of circular test structures spanning two orders of magnitude in diameter which we fabricated on the same diamond sample (Supplementary Fig. 3). Similar contrast improvements have previously been observed in quantum sensing

measurements utilizing NV^- ensembles¹⁹ and may result from a reduced contribution of out-of-focus fluorescence to the signal due to reduced reflections at the diamond top surface.

195

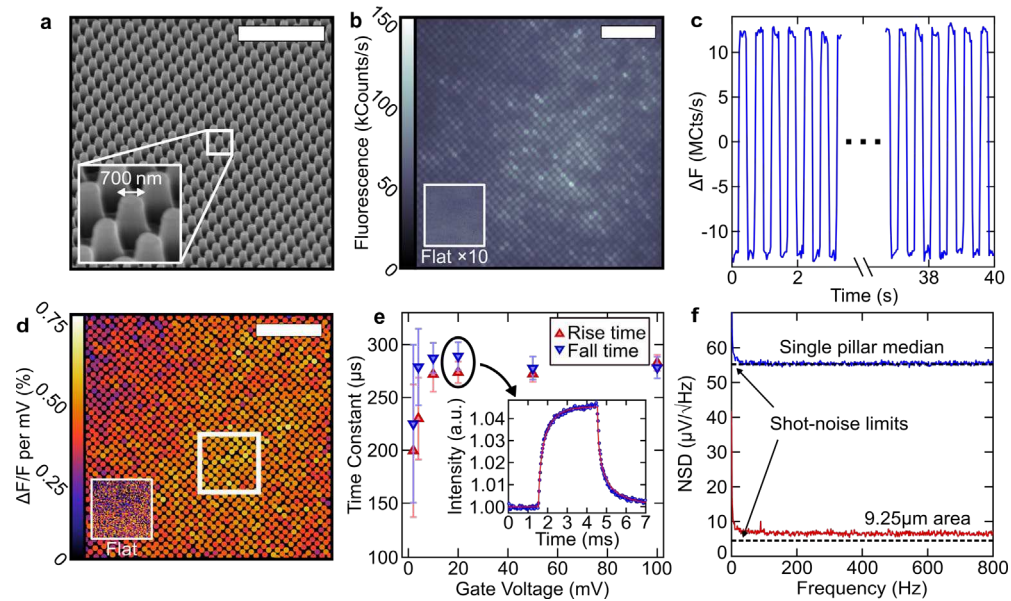


Fig. 3. Characterization of voltage-sensitive diamond optrode array. (a) Scanning-electron micrograph of the fabricated diamond optrodes. (b) Fluorescence image of the optrode array. (c) Change in fluorescence from an approximately $13.74\mu\text{m}\times 13.74\mu\text{m}$ section of the array shown in (b) resulting from the application of a 2Hz, 20mV square wave voltage in PBS over 40s. See Supplementary Fig.4 for full trace. (d) Map of fluorescence responsivity values for each optrode shown in (b). (e) Fluorescence rise and fall time-constants for the optrodes vs. square voltage pulse amplitude in solution. Error bars are one standard error in the fit parameters. Inset: representative response time-trace for a 20 mV pulse. 500 integrations were performed. Red lines are stretched exponential fits discussed in the Supplementary Information. (f) Noise power spectral densities from a single diamond optrode (blue, top) and the square area highlighted in (d) (red, bottom). Calculated shot noise limited sensitivities are indicated by dashed lines. Scale bars are $10\mu\text{m}$. These measurements were performed in highly conductive PBS (Methods).

200

205

To evaluate the temporal response of the DVIM, an avalanche photodiode was used to capture the fluorescence dynamics from the illuminated area upon application of 3ms square voltage pulses with varying amplitude from the large platinum counter electrode. Unlike the microelectrode measurements described above, here we used a highly conductive buffered saline solution to

210

minimize the RC time constant of the overall circuit. Fig. 3e shows the extracted rise and fall time constants, while the inset displays a representative fluorescence response time-trace. These responses are well fit by exponential functions and yield time constants consistent with capacitive charging of the diamond surface rather than NV charge state transition rates, which are expected to be $< 1\mu\text{s}$ ²⁶. As this charging time is limited by the diamond surface resistivity, it could be reduced in future devices by fabricating surface electrical contacts closer to the sensing region. The measured fluorescence response time of $< 300\mu\text{s}$ corresponds to a maximal operating frequency of around 3kHz. This knowledge allows us to reliably measure the noise spectral density of the DVIM while operating our camera at its highest possible framerate (over 128×128 pixels) of 1.6kHz. Fig. 3f displays the noise spectral density of a single optrode and a $9.25\mu\text{m} \times 9.25\mu\text{m}$ area (white square in Fig. 3d). Above $\approx 10\text{Hz}$, the measured noise floors show no apparent dependence on frequency and are consistent with the photon shot noise limits predicted by equation (1), which are denoted by dashed lines.

DVIM Sensitivity

From the measured noise power spectra, we obtain a sensitivity of $55\mu\text{V}/\sqrt{\text{Hz}}$ per optrode or $77\mu\text{V}\cdot\mu\text{m}/\sqrt{\text{Hz}}$, accounting for the inter-pillar pitch of $1.4\mu\text{m}$. This value, more than 6 times the sensitivity of the un-patterned area of the same sample, could be further improved to $42\mu\text{V}\cdot\mu\text{m}/\sqrt{\text{Hz}}$ by reducing the pitch to 900nm and utilizing hexagonal close-packed arrays in future devices. Diamond nanopillar structures are particularly attractive for electrophysiological applications due to their ability to facilitate close contact with cultured neurons¹⁶. With this use case in mind, Fig. 4a compares our measured optrode sensitivities to established technologies for voltage imaging of neuronal cultures *in vitro*. The sensitivity of DVIM technology (red and blue squares) lies below the threshold for intracellular neuronal recording at single-optrode resolution,

but is not presently sufficient for (real-time) high-resolution extracellular measurements. To gauge
235 the prospects for voltage sensing using charge state modulation of diamond color centers, we
estimate a technologically feasible upper limit on the sensitivity of a single diamond optrode using
 $NV^{0/+}$ sensing (green square) based on the implementation of established material and apparatus
optimizations (Supplementary Note 3). The limit of sensitivity using charge state interconversion
between NV^0 and NV^+ of around $375\text{ nV}/\sqrt{\text{Hz}}$ for a single optrode (Supplementary Fig. 5) is
240 comparable to state-of-the-art HD-MEAs, but offers more than one order of magnitude greater
spatial resolution. In addition, our optical readout mechanism is not subject to the same restrictions
on the total number of active recording channels as MEAs³⁷, potentially allowing higher volumes
of information to be extracted from dense neuronal cultures.

To model local bioelectrical charge injection and verify our calculated sensitivities, we developed
245 a protocol to generate voltage signals at the diamond surface with timescales and amplitudes
commensurate with neuronal activity. This was achieved in three steps: First, a micromanipulator
was used to maneuver a platinum/iridium microelectrode to within $2\mu\text{m}$ of the sensor surface.
Secondly, the solution conductivity was adjusted from pure deionized water by adding PBS until
signals applied by the microelectrode elicited a sub-millisecond fluorescence response. Finally, to
250 compensate for the shunting of injected charge to the solution ground and the spatial fall-off of the
signal produced by the microelectrode³⁸, the amplitude of the applied voltage signal was increased
until potential changes equivalent to measured intracellular²¹ action potential events were detected.
Fig. 4b shows the detection of 30mV, 1 ms square voltage pulses applied at a 10Hz repetition rate
(400mV applied to the microelectrode) over a 4×4 optrode array. This restricted area
255 ($5.6\mu\text{m}\times 5.6\mu\text{m}$) allowed for a camera recording rate of 2kHz, sufficient to observe sub-
millisecond fluorescence response times (Supplementary Fig. 6). We also note that the applied

signal was resolvable at the single-optrode level (Supplementary Fig. 6). To demonstrate that sub-millivolt detection is presently only limited by photon shot noise, we gated our measurements to the applied signals and averaged the results over several trials, a practice for which precedent exists for high-resolution mapping of extracellular signal propagation^{38,39}. Fig. 4c shows the resulting detected voltage traces integrated over a flat region ($1.7\mu\text{m}\times 1.7\mu\text{m}$), indicating a peak voltage of less than $800\mu\text{V}$ at the sensor surface (5mV applied to the microelectrode). The region of interest can also be broken into sixteen 425nm sub-regions, thereby demonstrating voltage recording with sub-micron resolution. This represents a 20 times improvement over current HD-MEA systems and is less than twice the diffraction limit of our microscopy apparatus ($\approx 230\text{nm}$). The averaged result of 2000 trials is shown in Fig. 4c for clarity, but we note that the signal was resolvable after only around 200 trials (Supplementary Fig. 6).

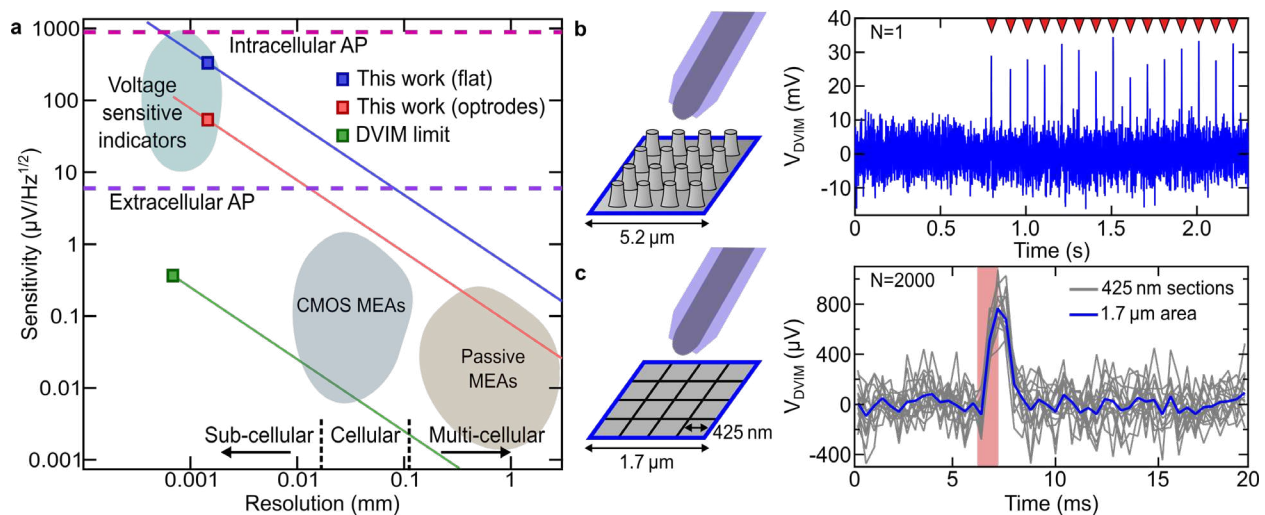


Fig. 4. Comparison to existing neuronal voltage imaging technology and demonstration of fast signal detection.

(a) Comparison of voltage sensitivities and signal detection thresholds at 1 kHz. Data points represent best measured sensitivities of flat (blue) and nano-patterned (red) DVIMs and the theoretical best sensitivity of a DVIM (green). Solid lines show the scaling of sensitivity with interrogated area (resolution) to assist with comparison to other technologies. Dashed horizontal lines show estimated detection thresholds for intracellular (pink, top) and extracellular (violet, middle) mammalian neuronal action potentials. Shaded regions roughly indicate the sensitivity and resolution regimes

available to current high-speed voltage imaging technologies (see Supplementary Note 2 for justification). (b) Detection of 1ms square voltage pulses applied with a platinum microelectrode at a repetition rate of 10Hz by a 4×4 array of optrodes (effective resolution of 5.2μm). Red triangles indicate the rising edges of the applied pulses. (c) Detection of 1ms square pulses with sub-mV amplitude and 425nm resolution by repeated integration on a 1.7μm×1.7μm section of a flat DVIM chip. The shaded region indicates the duration of the applied pulse. All displayed traces are unfiltered.

Discussion

We have demonstrated an optical voltage imaging sensor with a quantitative linear response utilizing the transitions of diamond NV centers between their neutral and positive charge states. Our method is made possible through tailored control over the NV ensemble charge state populations via electrochemical tuning of the diamond surface termination. This technology circumvents the need for on-chip readout circuitry, enabling resolutions more than twenty times higher than CMOS HD-MEAs while enabling parallel readout from, in principle, as many channels as there are pixels available on modern scientific cameras (> 1 million). Diamond voltage imaging microscopy can be immediately utilized in fundamental studies where the complex electrokinetic dynamics of diffuse liquids⁴⁰ preclude or complicate the use of single-point probe measurements⁴¹⁻⁴³, and may enable time-resolved imaging studies of battery systems^{24,25}. On the near-term horizon, our demonstration that nanopillar waveguides enhance sensitivity, combined with the previously demonstrated biocompatibility of similar diamond structures with neuronal cultures¹⁶, suggests that optrodes with diameters below 200nm may be used to enable intracellular access for electrophysiological recording²¹. Practical application of this technique to electrophysiology will likely require adhesion-promoting coatings to improve cell survival rates⁴⁴ and enhance signal strength via biological seal resistance²². The cationic nature of these coatings could conceivably cause changes to near-surface NV responses⁴⁵, however our testing has shown no deleterious

300 effects (Supplementary Note 4). Long-term photostability, the rapid response of NV emissions,
and the transparency of diamond make DVIMs an attractive platform for future studies of neuronal
network formation and function, where the transparent substrate can be leveraged to enable multi-
modal voltage imaging with, for instance, transcriptional^{46,47}, structural⁴⁸, or metabolomic⁴⁹ tags,
as well as all-optical closed-loop systems utilizing optogenetic stimulation^{50,51}. Building on the
305 physical understanding presented here, we predict that further optimization of this technology will
enable extracellular imaging of neuronal network dynamics with sub-micron resolution.

Acknowledgments: We thank Wei Tong for providing poly-D-lysine and assisting with the
coating process. We thank G. Berecki and S. Petrou for helpful discussions. D.S and L.T.H were
supported by the Australian Research Council (ARC) through Discovery Project 200103712. A.S
310 was supported by the ARC through DECRA 190100336. A.N was supported by the ARC through
Linkage 190100528. L.C.L.H was supported by the ARC Centre of Excellence for Quantum
Computation and Communication Technology. D.J.M was supported by an Australian
Government Graduate Research Training Scholarship. This work was performed in part at the
Melbourne Centre for Nanofabrication (MCN) in the Victorian Node of the Australian National
315 Fabrication Facility (ANFF).

Author contributions: D.J.M, N.D, and D.A.S developed the technological concepts and
designed the experiments with input from A.S, S.P, and L.C.L.H. The devices were designed and
fabricated by D.J.M and N.D with input from A.N. A.S performed the hydrogen-termination with
input from D.J.M. C.P performed the electrochemical oxidation procedure with input from D.J.M
320 and N.D. Microelectrode measurements and corresponding data analysis were performed by D.J.M
and N.D with input from L.T.H. The equivalent circuit model was developed by D.J.M. Optrode
array measurements and data analysis were performed by D.J.M with input from N.D and L.T.H.

D.J.M, N.D, and D.S wrote the original manuscript draft. All authors contributed to reviewing and editing the manuscript. L.C.L.H, S.P, and D.A.S supervised the work.

325 **Competing interests:** D.J.M, N.D, A.S, and D.A.S are authors on a provisional patent granted to The University of Melbourne covering the fabrication of the NV⁰⁺ ensemble chip and its use in voltage sensing applications (IP Australia patent no. 2021901331).

Data availability: Data, custom analysis code, and simulation code are available from the corresponding authors upon reasonable request.

330

Additional information:

Supplementary information is available for this paper at [address]

Correspondence and requests for materials should be addressed to D.J.M or D.A.S.

Methods

335 **Sensor Fabrication:** High density near-surface NV ensembles were created via 2keV implants of ¹⁴N ions at a dose of 10¹³/cm² and an incidence angle of 7° (InnovIon) into commercial CVD electronic-grade <100> diamond wafers (Element Six) following the procedures outlined in previous works⁵². The samples were initially oxygen-terminated by boiling in a hot mixture of sulphuric acid and sodium nitrate for 30 minutes. Ti/Pt 15/50nm electrical contacts were patterned
340 on the diamond surface via photolithography using TI35E resist in image reversal mode. Nanopillar arrays were fabricated via electron-beam lithography and oxygen plasma reaction-ion etching using our previously reported method¹⁹. Samples were indirectly exposed to a hydrogen plasma in a PECVD diamond growth reactor (Seki), where indirect exposure was achieved by shielding the samples from the plasma ball with a perforated molybdenum shell (Supplementary
345 Fig. 1).

Sensitization and Characterization: Custom-built fluid wells were fabricated by patterning glass coverslips with a thickness of 50 μ m with a platinum ring counter electrode and a platinum stripline for contacting the diamond samples. The coverslips were attached to custom printed-circuit boards with circular cutouts using commercial two-part epoxy resin. Silicone fluid wells were made by
350 pouring two-part silicone rubber into custom molds. The bases of the molds were flat enough that the resulting silicone wells would spontaneously form a watertight seal on contact with the glass coverslips. Samples were mounted to the coverslips with a thin layer of optically transparent, non-fluorescent silicone rubber (Sylgard 184 from Dow Corning) and electrical contact between the samples and platinum stripline was made using conductive silver epoxy (CircuitWorks). The cured
355 silver epoxy was then encapsulated with silicone to prevent Faradaic short-circuiting of applied voltage signals through solution.

All voltage signals used in this work were applied using a Rigol DG4162 Function/Arbitrary Waveform Generator. The diamond devices were sensitized in phosphate buffered saline solution
360 (PBS - 137mM NaCl, 10mM Phosphate, 2.7mM KCl, pH 7.4, and osmolality of 280-310mOsm/kg, Gibco Thermo Fisher Australia) by the repeated application of oxidative voltage pulses (Fig. 1e) applied between a platinum counter electrode and the diamond until device sensitivity plateaued. Sensitivity was calculated from measured fluorescence responses to 50mV peak-to-peak square pulses applied through the counter electrode using equation (1). For
365 microelectrode experiments, commercial deionized water (Honeywell) was mixed with a small amount of PBS to create a dilute conductive solution in which to perform the measurements. The microelectrode (rounded tip Pt/Ir electrode from Microprobes for Life Science) was positioned just above the diamond surface using a manual micromanipulator by first bringing the tip into contact with the surface as determined by a local change in diamond fluorescence at the tip location due

370 to contact potential difference. The tip was then lifted off the surface until the local fluorescence
change vanished and was allowed to settle for 20 minutes prior to measurement to ensure that no
movement of the electrode occurred during recording. Through brightfield imaging of the
microelectrode (Fig. 2a) we confirmed that the tip was situated within half the focal depth of our
microscope objective from the surface (approximately $5\mu\text{m}$).

375

Fluorescence Measurements: Fluorescence was excited with a 200mW, 532nm laser (Coherent
Verdi) and collected through either a coverslip-corrected air objective with a $20\times$ magnification
(NA 0.8, roughly $0.3\text{kW}/\text{cm}^2$) for microelectrode imaging measurements or an oil-immersion
objective with $40\times$ magnification (NA 1.4, roughly $0.6\text{kW}/\text{cm}^2$) for optrode array measurements,
380 chip sensitization, and per-area sensitivity measurements. For per-area sensitivity measurements,
only a small area at the center of the excitation laser spot where diamond fluorescence was
brightest was considered for both the optrode array (highlighted region in Fig. 3d) and flat surface
(inset in Fig. 3d). Collected light was split with a 530nm dichroic mirror and filtered with either a
580nm long-pass (camera measurements, spectra in Fig. 1h) or a 545nm long-pass (spectra in Fig.
385 1b). Spectroscopy was performed with a fiber-coupled spectrometer (OceanInsight FLAME),
while fluorescence video was recorded using an sCMOS camera (ANDOR Neo) which was
thermoelectrically cooled to -40°C . Avalanche photodiode (APD) measurements were performed
with a fiber-coupled single-photon counting unit (Excelitas Technologies). Spectrometer and
camera readings were corrected by subtraction of background/dark counts measured without laser
390 illumination. Diamond fluorescence spectra in Fig. 1b have had diamond Raman scattering and
non-diamond background fluorescence removed for clarity, the original spectra are shown in
Supplementary Fig. 1.

Raw fluorescence images $F(t)$ with a solution gate voltage applied were converted to fluorescence
 395 contrast f_c images via:

$$f_c = \frac{\Delta F}{F_0}$$

Where $\Delta F = \langle F(t) - F_0 \rangle$, and F_0 is the baseline fluorescence measured with the sensor and any
 external electrodes grounded.

Voltage Response Characterization: DVIM voltage response calibration was performed with
 400 voltages applied between the large platinum counter electrode (Fig. 1a) and the sensor. For
 microelectrode measurements, calibration was performed in the same dilute solution as the
 recordings, although produced similar responses to calibrations in PBS. The voltage was stepped
 15 times in increments of 10mV, from 0V to -70mV, then to 70mV and back to 0V, with a step
 405 period of ≈ 25 s. The sensor fluorescence was recorded over a 768×768 pixel region at 10 frames
 per second. Pixels in the calibration video were binned to match the binning of pixels in the
 processed recording data (32×32 pixels for data displayed in Fig. 2). For each pixel the average
 fluorescence for the last 15s of each voltage step was fit as a linear function of the applied voltage
 using least squares regression (polyfit from the python NumPy library) to extract gradients m and
 410 offsets b of the linear functions as well as the covariance matrix for the fit Γ . Per-pixel fluorescence
 contrasts f_c and uncertainties δf_c were then calculated via:

$$f_c = -m/b,$$

$$(\delta f_c)^2 \approx \left(\frac{\partial f_c}{\partial m}\right)^2 (\sigma_m)^2 + \left(\frac{\partial f_c}{\partial b}\right)^2 (\sigma_b)^2 + 2 \left(\frac{\partial f_c}{\partial b}\right) \left(\frac{\partial f_c}{\partial m}\right) (\sigma_{b,m})^2$$

415

Where the covariance matrix $\Gamma = \begin{pmatrix} \sigma_m & \sigma_{b,m} \\ \sigma_{b,m} & \sigma_b \end{pmatrix}$.

420 Calibration was performed in PBS for optrode array measurements. 2Hz square waves with one half-period at 0V and the other half-period at $\pm 2\text{mV}$, $\pm 5\text{mV}$, and from $\pm 10\text{mV}$ to $\pm 50\text{mV}$ (steps of 10mV) were applied for 10s. Fluorescence was recorded over 1024×1024 pixel regions at ≈ 10 frames per second. The pixels belonging to each optrode were binned using a circular Hough transform algorithm⁴⁶⁴⁶⁴⁶ prior to further processing. The fluorescence histogram of each optrode was fit with the sum of two Gaussian lineshapes, $g(x, \bar{x}_1, \bar{x}_2, \sigma_1, \sigma_2, A_1, A_2)$, where \bar{x} , σ , and A denote the mean, standard-deviation, and integrated area of each Gaussian, using the nonlinear
425 least-squares curve fitting function available from the `scipy.optimize` library. The per-optrode fluorescence contrast and its uncertainty were then computed via:

$$f_c = 2 \frac{\bar{x}_1 - \bar{x}_2}{\bar{x}_1 + \bar{x}_2}$$

$$(\delta f_c)^2 \approx (\sigma_1)^2 + (\sigma_2)^2$$

430

The fluorescence contrast responsivity was then calculated by fitting straight line functions with a zero-intercept to f_c as a function of the excursion voltage from 0V (Supplementary Fig. 3).

435 Radial averages in Fig. 2f were weighted with the estimated standard deviation (quadrature sum of percentage contrast error δf_c and estimated per-pixel noise). The radius assigned to a pixel was calculated as integer floor of the true radius at the inner-most corner of each pixel (with respect to the pixel chosen as the center point). The error bars shown are 95% confidence intervals determined from the student's t-distribution using a weighted radial standard deviation.

440 **Fitting of Avalanche Photodiode Measurements:** Measurements of the DVIM response time in
 PBS performed with an APD used aggregate fluorescence collected from an $\approx 200\mu\text{m}$ circular
 illuminated region of the sample. Due to the finite conductivity of the hydrogen-terminated
 diamond surface, we expect the fluorescence response of the DVIM (which results from the re-
 equilibration of the two-dimensional hole gas density in response to a change in the density of
 445 solvated charges at the diamond surface) to exhibit an RC-like time-constant. However, the
 varying proximity of each point in the illuminated area to the Ti/Pt electrical contact on the sample
 surface means we also expect a small amount of variation in the equilibration time constant
 between each point. To capture this effect on the aggregate fluorescence measured with the APD,
 we fit the measured response curves with stretched exponential functions which can account for a
 450 distribution of response times within the illuminated area⁵⁴. These functions $S(t)$ take the form:

$$S_{rise}(t) = \alpha \left(1 - e^{\left(\frac{-t}{\tau_{rise}}\right)^\gamma} \right)$$

$$S_{fall}(t) = \alpha e^{\left(\frac{-t}{\tau_{fall}}\right)^\gamma}$$

455 Where α is the fluorescence contrast, t is the time following the start (for $S_{rise}(t)$) or end (for
 $S_{fall}(t)$) of the voltage pulse, $\tau_{rise/fall}$ are the fluorescence rise/fall time constants, and γ is the
 stretch factor.

References:

- 460
1. Knöpfel, T. & Song, C. Optical voltage imaging in neurons: moving from technology development to practical tool. *Nature Reviews Neuroscience* **20**, (2019).
 2. Piatkevich, K. D. *et al.* Population imaging of neural activity in awake behaving mice. *Nature* **574**, (2019).
 3. Wang, W., Kim, C. K. & Ting, A. Y. Molecular tools for imaging and recording neuronal activity. *Nature Chemical Biology* **15**, (2019).

- 465 4. Abdelfattah, A. S. *et al.* Bright and photostable chemigenetic indicators for extended in vivo voltage imaging. *Science* **365**, (2019).
5. Abbott, J. *et al.* Extracellular recording of direct synaptic signals with a CMOS-nanoelectrode array. *Lab on a Chip* **20**, (2020).
6. Emmenegger, V., Obien, M. E. J., Franke, F. & Hierlemann, A. Technologies to Study Action Potential Propagation With a Focus on HD-MEAs. *Frontiers in Cellular Neuroscience* **13**, (2019).
- 470 7. Castelletto, S. & Boretti, A. Color centers in wide-bandgap semiconductors for subdiffraction imaging: a review. *Advanced Photonics* **3**, (2021).
8. Lühmann, T. *et al.* Screening and engineering of colour centres in diamond. *Journal of Physics D: Applied Physics* **51**, (2018).
9. Petrakova, V. *et al.* Charge-sensitive fluorescent nanosensors created from nanodiamonds. *Nanoscale* **7**, 12307–12311 (2015).
- 475 10. Karaveli, S. *et al.* Modulation of nitrogen vacancy charge state and fluorescence in nanodiamonds using electrochemical potential. *Proceedings of the National Academy of Sciences* **113**, (2016).
11. Doherty, M. W. *et al.* The nitrogen-vacancy colour centre in diamond. *Physics Reports* **528**, (2013).
- 480 12. Schirhagl, R., Chang, K., Loretz, M. & Degen, C. L. Nitrogen-Vacancy Centers in Diamond: Nanoscale Sensors for Physics and Biology. *Annual Review of Physical Chemistry* **65**, (2014).
13. Grotz, B. *et al.* Charge state manipulation of qubits in diamond. *Nature Communications* **3**, (2012).
14. Krečmarová, M. *et al.* A Label-Free Diamond Microfluidic DNA Sensor Based on Active Nitrogen-Vacancy Center Charge State Control. *ACS Applied Materials & Interfaces* **13**, (2021).
- 485 15. Yang, K.-H. & Narayan, R. J. Biocompatibility and functionalization of diamond for neural applications. *Current Opinion in Biomedical Engineering* **10**, (2019).
16. Hanlon, L. *et al.* Diamond nanopillar arrays for quantum microscopy of neuronal signals. *Neurophotonics* **7**, (2020).
17. Momenzadeh, S. A. *et al.* Nanoengineered Diamond Waveguide as a Robust Bright Platform for Nanomagnetometry Using Shallow Nitrogen Vacancy Centers. *Nano Letters* **15**, (2015).
- 490 18. Kehayias, P. *et al.* Solution nuclear magnetic resonance spectroscopy on a nanostructured diamond chip. *Nature Communications* **8**, (2017).
19. McCloskey, D. J. *et al.* Enhanced Widefield Quantum Sensing with Nitrogen-Vacancy Ensembles Using Diamond Nanopillar Arrays. *ACS Applied Materials and Interfaces* **12**, (2020).
- 495 20. Abbott, J. *et al.* A nanoelectrode array for obtaining intracellular recordings from thousands of connected neurons. *Nature Biomedical Engineering* **4**, (2020).
21. Liu, R. *et al.* High Density Individually Addressable Nanowire Arrays Record Intracellular Activity from Primary Rodent and Human Stem Cell Derived Neurons. *Nano Letters* **17**, (2017).
22. Spira, M. E. & Hai, A. Multi-electrode array technologies for neuroscience and cardiology. *Nature Nanotechnology* **8**, (2013).
- 500 23. Stotter, J., Show, Y., Wang, S. & Swain, G. Comparison of the Electrical, Optical, and Electrochemical Properties of Diamond and Indium Tin Oxide Thin-Film Electrodes. *Chemistry of Materials* **17**, (2005).
24. Kempaiah, R., Vasudevamurthy, G. & Subramanian, A. Scanning probe microscopy based characterization of battery materials, interfaces, and processes. *Nano Energy* **65**, (2019).
- 505 25. Liu, D. *et al.* Evolution of Solid Electrolyte Interface on TiO₂ Electrodes in an Aqueous Li-Ion Battery Studied Using Scanning Electrochemical Microscopy. *The Journal of Physical Chemistry C* **123**, (2019).
26. Schreyvogel, C., Polyakov, V., Wunderlich, R., Meijer, J. & Nebel, C. E. Active charge state control of single NV centres in diamond by in-plane Al-Schottky junctions. *Scientific Reports* **5**, (2015).
27. Stacey, A. *et al.* Depletion of nitrogen-vacancy color centers in diamond via hydrogen passivation. *Applied Physics Letters* **100**, (2012).
- 510 28. Findler, C., Lang, J., Osterkamp, C., Nesládek, M. & Jelezko, F. Indirect overgrowth as a synthesis route for superior diamond nano sensors. *Scientific Reports* **10**, 22404 (2020).
29. Ristein, J. Surface transfer doping of diamond. *Journal of Physics D: Applied Physics* **39**, (2006).
30. Maier, F., Riedel, M., Mantel, B., Ristein, J. & Ley, L. Origin of Surface Conductivity in Diamond. *Physical Review Letters* **85**, 3472–3475 (2000).
- 515 31. Broadway, D. A. *et al.* Spatial mapping of band bending in semiconductor devices using in situ quantum sensors. *Nature Electronics* **1**, (2018).
32. Chaplin, B. P., Hubler, D. K. & Farrell, J. Understanding anodic wear at boron doped diamond film electrodes. *Electrochimica Acta* **89**, (2013).
- 520 33. Petraková, V. *et al.* Luminescence of Nanodiamond Driven by Atomic Functionalization: Towards Novel Detection Principles. *Advanced Functional Materials* **22**, 812–819 (2012).

34. Ristein, J., Zhang, W. & Ley, L. Hydrogen-terminated diamond electrodes. I. Charges, potentials, and energies. *Physical Review E* **78**, (2008).
- 525 35. Licht, Stuart., Cammarata, Vince. & Wrighton, M. S. Direct measurements of the physical diffusion of redox active species: microelectrochemical experiments and their simulation. *The Journal of Physical Chemistry* **94**, (1990).
36. Dankerl, M. *et al.* Hydrophobic Interaction and Charge Accumulation at the Diamond-Electrolyte Interface. *Physical Review Letters* **106**, 196103 (2011).
37. Ogi, J. *et al.* A 4.8- μ Vrms-Noise CMOS-Microelectrode Array With Density-Scalable Active Readout Pixels via Disaggregated Differential Amplifier Implementation. *Frontiers in Neuroscience* **13**, (2019).
- 530 38. Viswam, V., Obien, M. E. J., Franke, F., Frey, U. & Hierlemann, A. Optimal Electrode Size for Multi-Scale Extracellular-Potential Recording From Neuronal Assemblies. *Frontiers in Neuroscience* **13**, (2019).
39. Müller, J. *et al.* High-resolution CMOS MEA platform to study neurons at subcellular, cellular, and network levels. *Lab on a Chip* **15**, (2015).
40. Bazant, M. Z., Thornton, K. & Ajdari, A. Diffuse-charge dynamics in electrochemical systems. *Physical Review E* **70**, (2004).
- 535 41. Collins, L., Kilpatrick, J. I., Kalinin, S. v & Rodriguez, B. J. Towards nanoscale electrical measurements in liquid by advanced KPFM techniques: a review. *Reports on Progress in Physics* **81**, (2018).
42. Collins, L. *et al.* Full data acquisition in Kelvin Probe Force Microscopy: Mapping dynamic electric phenomena in real space. *Scientific Reports* **6**, (2016).
- 540 43. Salerno, M. & Dante, S. Scanning Kelvin Probe Microscopy: Challenges and Perspectives towards Increased Application on Biomaterials and Biological Samples. *Materials* **11**, (2018).
44. Garrett, D. J., Tong, W., Simpson, D. A. & Meffin, H. Diamond for neural interfacing: A review. *Carbon* **102**, 437–454 (2016).
- 545 45. Petrakova, V. *et al.* Imaging of transfection and intracellular release of intact, non-labeled DNA using fluorescent nanodiamonds. *Nanoscale* **8**, 12002–12012 (2016).
46. Kitagawa, H. *et al.* Activity-Dependent Dynamics of the Transcription Factor of cAMP-Response Element Binding Protein in Cortical Neurons Revealed by Single-Molecule Imaging. *The Journal of Neuroscience* **37**, (2017).
- 550 47. Wu, B., Eliscovich, C., Yoon, Y. J. & Singer, R. H. Translation dynamics of single mRNAs in live cells and neurons. *Science* **352**, (2016).
48. Lukinavičius, G. *et al.* Fluorogenic probes for live-cell imaging of the cytoskeleton. *Nature Methods* **11**, (2014).
49. Zhang, Z., Chen, W., Zhao, Y. & Yang, Y. Spatiotemporal Imaging of Cellular Energy Metabolism with Genetically-Encoded Fluorescent Sensors in Brain. *Neuroscience Bulletin* **34**, (2018).
- 555 50. Barral, J. & D Reyes, A. Synaptic scaling rule preserves excitatory–inhibitory balance and salient neuronal network dynamics. *Nature Neuroscience* **19**, (2016).
51. Werley, C. A., Chien, M.-P. & Cohen, A. E. Ultrawidefield microscope for high-speed fluorescence imaging and targeted optogenetic stimulation. *Biomedical Optics Express* **8**, (2017).
- 560 52. Tetienne, J.-P. *et al.* Spin properties of dense near-surface ensembles of nitrogen-vacancy centers in diamond. *Physical Review B* **97**, (2018).
53. Smereka, M. & Dulęba, I. Circular Object Detection Using a Modified Hough Transform. *International Journal of Applied Mathematics and Computer Science* **18**, (2008).
54. Hall, L. T. *et al.* Detection of nanoscale electron spin resonance spectra demonstrated using nitrogen-vacancy centre probes in diamond. *Nature Communications* **7**, (2016).

565

Supplementary Files

This is a list of supplementary files associated with this preprint. Click to download.

- [SupplementaryVideo1.mp4](#)
- [DMcCloskey2021DVIMSIRev1.pdf](#)